Deep tissue volumetric optoacoustic tracking of individual circulating tumor cells in an intracardially perfused mouse model ⓇCrossMark

Xosé Luís Deán-Ben [a,b,*,1]; Ina Weidenfeld [b,1];
Oleksiy Degtyaruk [a,b,1]; Vasilis Ntziachristos [b];
Andre C. Stiel [b]; Daniel Razansky [a,b]

[a] Institute for Biomedical Engineering and Institute of Pharmacology and Toxicology, University of Zurich and ETH Zurich, Switzerland; [b] Institute of Biological and Medical Imaging (IBMI), Technical University of Munich and Helmholtz Center Munich, Germany

Abstract

Widespread metastasis is the major cause of death from melanoma and other types of cancer. At present, the dynamic aspects of the metastatic cascade remain enigmatic. The feasibility to track circulating melanoma cells deep within living intact organisms can greatly impact our knowledge on tumor metastasis, but existing imaging approaches lack the sensitivity, spatio-temporal resolution or penetration depth to capture flowing tumor cells over large fields of view within optically-opaque biological tissues. Vast progress with the development of optoacoustic tomography technologies has recently enabled two- and three-dimensional imaging at unprecedented frame rates in the order of hundreds of Hertz, effectively mapping up to a million image voxels within a single volumetric snapshot. Herein, we employ volumetric optoacoustic tomography for real-time visualization of passage and trapping of individual B16 melanoma cells in the whole mouse brain. Detection of individual circulating melanoma cells was facilitated by substituting blood with an artificial cerebrospinal fluid that removes the strong absorption background in the optoacoustic images. The approach can provide new opportunities for studying trafficking and accumulation of metastatic melanoma cells in different organs.

Neoplasia (2020) 22 441–446

Introduction

Malignant melanomas are very aggressive tumors responsible for almost 60% of deaths from skin cancer [1]. Melanomas originate from transformed melanocytes, which are pigment-producing cells present in the skin of humans and other mammals [2]. Melanoma cells tend to detach from the primary tumor and enter the bloodstream to become highly invasive and metastatic at secondary sites in the body [3]. To this end, significant efforts have been invested into studying the steps involved in metastasis, yet this process remains one of the most enigmatic aspects of cancer progression [4]. One major reason behind this knowledge gap is lack of suitable imaging tools capable of visualizing dynamic biological processes deep in an intact living organism with sufficient spatiotemporal resolution [5]. Since tumors mainly disseminate through the bloodstream, major advancement with development of new therapeutic strategies can be made by enabling direct observation of how tumor cells enter the vessels, extravasate in distant areas, adapt to new environments, eventually seeding and proliferating [6]. Tumor cells flowing within vascular structures are known as circulating tumor cells (CTCs). The latter have been studied as minimally invasive multifunctional bio-markers with promising prognostic value [7]. Indeed, reliable detection of CTC presence in blood may serve as a more reproducible indicator of disease status as compared to macroscopic tumor observations with conventional clinical imaging modalities, at least in some types of cancer [8]. Imaging of CTCs is technically challenged by the low sensitivity in detecting these rare cells in deep tissues. Even though melanin is a paramagnetic substance generating contrast in magnetic resonance imaging (MRI) [9,10], labelling is generally required to track cellular dissemination [11]. Additionally, CTCs have relatively large size with respect to the bores of capillaries and are expected to mainly trap in the capillary bed during the first pass [4]. Thereby, high-frame-imaging is required to capture their dynamics in blood and better understand their *in vivo* behavior.

Optoacoustic (OA) tomography has recently been advanced to attain ultrafast two- and three-dimensional imaging at rates of hundreds to thousands of frames per second [12–14]. By further capitalizing on its unique optical absorption contrast, OA has provided unprecedented insights into rapid biological processes, such as whole brain activity or cardiovascular dynamics [13,15,16]. The feasibility to detect primary melanomas and circulating melanoma cells by exploiting the endogenous contrast generated

* Corresponding author at: Institute for Biomedical Engineering and Institute of Pharmacology and Toxicology, University of Zurich and ETH Zurich, Switzerland.
e-mail address: xl.deanben@pharma.uzh.ch (Xosé Luís Deán-Ben).
[1] These authors contributed equally to this work.

by melanin has been demonstrated with early OA embodiments [17,18]. Cell labeling, magnetic trapping and proper selection of the detection bandwidth have subsequently facilitated more sensitive detection of flowing CTCs [19–22]. To this end, single cells can readily be detected with OA microscopy at shallow depths [23,24], while tomographic approaches have also been shown capable of resolving individual melanin-loaded cells [25]. Yet, dynamic visualization of individual flowing CTCs in large tissue volumes has not been achieved so far.

Herein, we employed volumetric OA tomography to dynamically track circulating melanoma cells at an imaging rate of 100 volumes per second and ∼200 μm spatial resolution across a field of view of ∼1 cm^3. The imaging scanner was combined with a cardiac perfusion system that substituted blood with an artificial cerebrospinal fluid (ACSF) to reduce the background light absorption and enable efficient detection of single cells. We then capitalized on the high sensitivity and spatio-temporal resolution of the OA tomography system to visualize how intracardially-injected B16 melanoma cells flow through the cerebral circulatory system and subsequently lodge in capillaries.

Results

Single-cell imaging in phantoms

The feasibility to detect OA signals generated by individual B16 melanoma cells and distinguish those in the OA images was first demonstrated by embedding sparsely distributed cells in an agar phantom. Lay-out of the experimental system is schematically depicted in Fig. 1a (see methods for a detailed description). Basically, the output light beam of a tunable optical parametric oscillator (OPO)-based laser was guided through a fiber bundle to illuminate an area of ∼4 mm diameter on the surface of the phantom (optical fluence <20 mJ/cm^2). The generated OA signals were detected with a custom-made 512-element spherical array coaxially aligned with the fiber bundle, which provides an almost isotropic resolution of ∼150 μm around the center of the sphere [26]. The volume enclosed between the phantom and the array surface was filled with agar to guarantee acoustic coupling. Fig. 1b shows the maximum intensity projection (MIP) along the depth direction of the reconstructed 3D OA image corresponding to excitation with a single laser pulse at 700 nm. The image exhibited a signal-to-noise ratio (SNR) of 22, calculated as the average intensity of 5 detectable dots relative to the standard deviation in a background region. A bright field microscopy image taken after OA imaging (Fig. 1c) was used to look through the entire agar layer and identify individual melanoma cells. Note that the OA resolution is inferior to the bright field images, hence the observed dots are significantly larger. Yet, the central positions of the dots match the positions of the isolated cells in the bright field image. This, along with the high SNR of the OA image, serves to verify that individual cells can be clearly detected and resolved. This is expected considering that B16 melanoma cells are large melanin-loaded cells with typical dimensions of ∼30 μm (inset in Fig. 1c). No significant photodamage associated to laser exposure was observed in the cells.

The basic capability to track flowing cells was additionally demonstrated with the same imaging set-up by embedding polyethylene tubing with 0.58 and 0.96 mm inner and outer diameters, respectively (Smiths Medical Inc. Minneapolis, USA), in agar and operating the laser at 100 Hz pulse repetition frequency (PRF). In order to mitigate image intensity fluctuations, the acquired signals were further normalized with the per-pulse laser photodiode energy readings provided by the laser. Fig. 1d shows a representative 3D view of the OA images acquired at 700 nm excitation wavelength for two consecutive time instants. Considering that the B16 cell solution was filtered with 35 μm mesh size before injection into the tubing, the dots in Fig. 1d clearly represent individual cells. In a practical scenario, the OA signal from melanoma cells is mixed

with a background signal mainly generated by blood. Fig. 1e displays the extinction coefficients of melanin and hemoglobin for different oxygen saturation (sO$_2$) levels. The ratio of extinction coefficients is shown in Fig. 1f, also as a function of sO$_2$. Black dots indicate the maxima of each curve. It is shown that the highest ratio is achieved for ∼680 nm at sO$_2$ = 100% while it converges to ∼730 nm at lower sO$_2$ levels. Considering typical sO$_2$ levels of 98% and 70% in arteries and veins, respectively, it appears that shorter wavelengths in the NIR window are more suitable for detecting circulating cells in the presence of blood. However, the light attenuation gets stronger at shorter wavelengths due to higher photon absorption and scattering, which needs to be taken into account when aiming at deep tissue penetration. Melanin may also be spectroscopically unmixed from OA images taken at multiple wavelengths. However, melanin features a monotonically decreasing absorption spectrum without distinctive peaks, which hampers its accurate unmixing. This range of wavelengths appears also to be appropriate to detect the cells in capillary networks featuring sO$_2$ values below 50% [27,28].

Cell tracking in mouse brain

An intracardially perfused mouse model was developed to physically remove the highly absorbing background of mammalian tissues and facilitate the detection of melanoma cells. Substitution of blood by oxygenated ACSF delivered at pressures of 100 þ 2 mmHg and physiological body temperature of 37 þ 0.5 °C enabled preserving functional activity resembling *in vivo* conditions for up to ∼45 min [29]. The perfusion and imaging set-up is sketched in Fig. 2a (see methods for a detailed description). OA images of the mouse brain were acquired during the entire perfusion procedure with the output wavelength and PRF of the laser set to 700 nm and 100 Hz, respectively. As expected, the background OA signal at the discernible vascular structures dropped significantly following perfusion (Fig. 2b), even though it appears that some blood tends to accumulate in the frontal part of the superior sagittal sinus. The perfusion procedure is best visualized in a movie showing the top-view MIPs of the reconstructed OA volumes provided in the on-line version of the journal (supplementary movie 1).

The feasibility to track B16 melanoma cells in the brain vascular network was demonstrated by filtering the B16 buffer (mesh size 35 μm) before injection through the 25 G butterfly needle inserted in the left ventricle. A total volume of 1000 μl containing approximately 2.5 million cells was injected. OA imaging was performed with the laser wavelength and PRF set to 700 nm and 50 Hz, respectively. Representative OA images (MIPs of the reconstructed 3D OA images along the depth direction) for several time points after injection of the melanoma cells are shown in Fig. 3a. The background signal levels in these images was rescaled with respect to Fig. 2b. Flowing cells are labelled with arrows, while stars represent cells that have been arrested in microvascular structures. The flow of cells is further illustrated in the top-view MIPs (supplementary movie 2) and rotating-view MIPs (supplementary movie 3) videos accompanying the on-line version of the manuscript. Fig. 3b displays the OA image (MIP along the depth direction) obtained after subtracting the average of 100 frames before cell injection for a time point when circulation of cells was no longer detected. In this way, signals originating from the cells can be effectively amplified via background removal. This approach may facilitate the visualization of cells *in vivo*. However, inter-frame motion of microvascular structures ascribed to respiratory and cardiac cycles as well as per-pulse laser fluctuations (in energy and beam shape) represent additional significant challenges. The resulting image obtained after background subtraction has an SNR of 19, calculated as the average intensity of the five labelled dots normalized by the standard deviation in the background region. This is consistent with the SNR values obtained in the phantom experiments considering the light attenuation associated with tis-
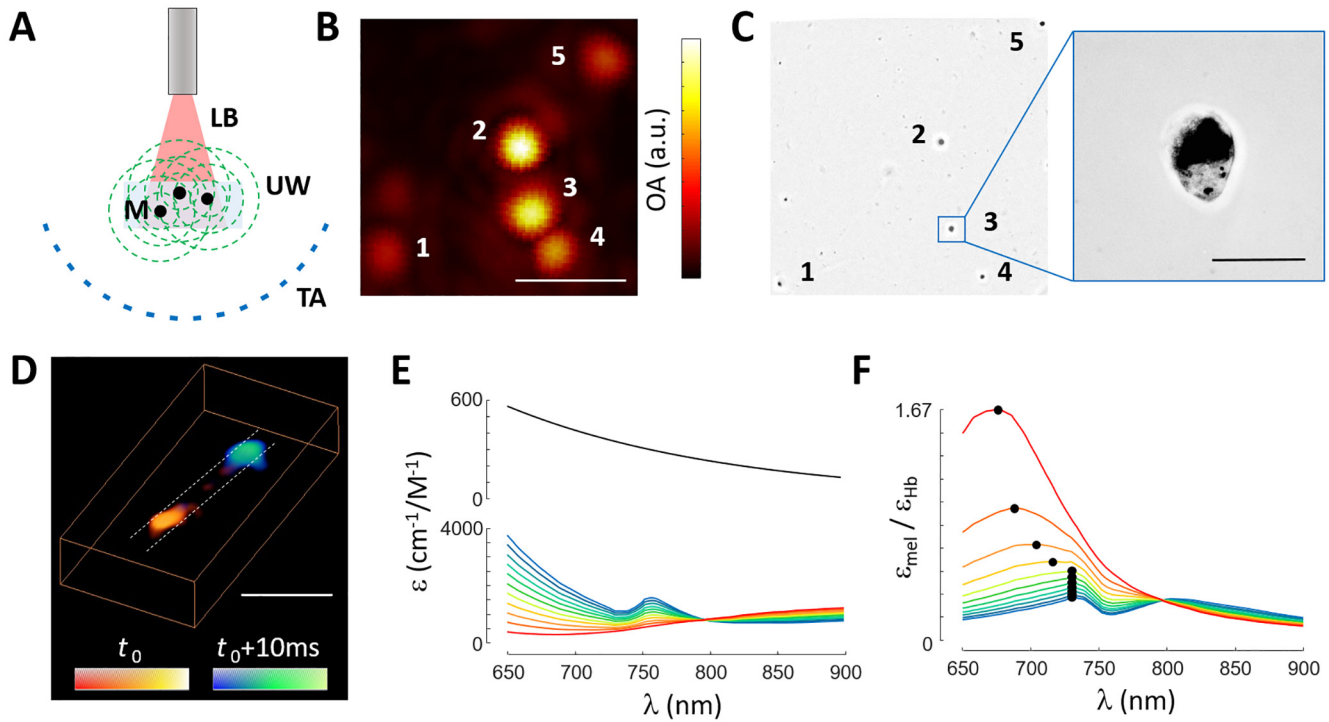
Fig. 1. Optoacoustic imaging of isolated cells. (a) Lay-out of the optoacoustic imaging system. M – B16 melanoma cells, LB – laser beam, UW – ultrasound waves, TA – transducer array. (b) Maximum intensity projection (MIP) of the three-dimensional optoacoustic image of isolated melanoma cells in agar. Scalebar – 1 mm. (c) Equivalent bright field microscopic image of the cells. Scalebar – 50 μm. (d). Three dimensional view of the optoacoustic images acquired at two consecutive instants for B16 cells flowing in a tubing. Scalebar – 2 mm. (e) Molar extinction coefficient (absorption spectrum) of melanin and hemoglobin as a function of the oxygen saturation (sO$_2$) level. (f) Ratio of the extinction coefficients in (e) as a function of sO$_2$.
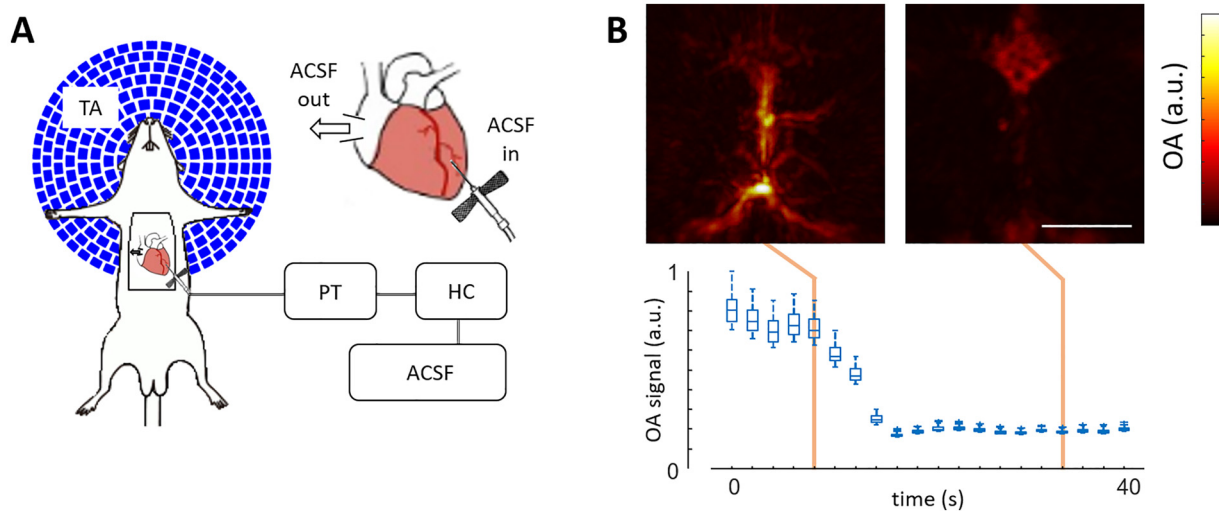

Fig. 2. Blood removal via intracardial perfusion. (a) Lay-out of the intracardiac perfusion model along with the optoacoustic imaging system. TA – transducer array, PT – pressure transducer, HC – heating coil, ACSF – artificial cerebrospinal fluid. (b) Maximum intensity projections (MIPs) of the three dimensional optoacoustic images taken before (left) and after (right) ACSF perfusion along with boxplots of the optoacoustic signals for the 100 brightest voxels in the image as a function of time. Scalebar – 3 mm.

sue absorption and scattering in the scalp and skull of the mouse. Two videos showing the MIPs of background-subtracted frames along with the reference anatomical image taken before intracardiac perfusion are also available in the on-line version of the journal (supplementary movie 4 and 5). Several B16 cells arrested in the cortical microvasculature were visible in the photograph of excised brain taken after the experiment (Fig. 3c). Their

relative locations match the positions of the dots detected in the OA image (labelled with arrows in Fig. 3b and c). Microscopic images of the cells marked in Fig. 3c are displayed in Fig. 3d. Those represent individual melanoma cells that were lodged in a superficial region accessible with optical microscopy. Other detected dots in the OA image may also represent individual cells, although melanoma cells can also circulate as microclusters.
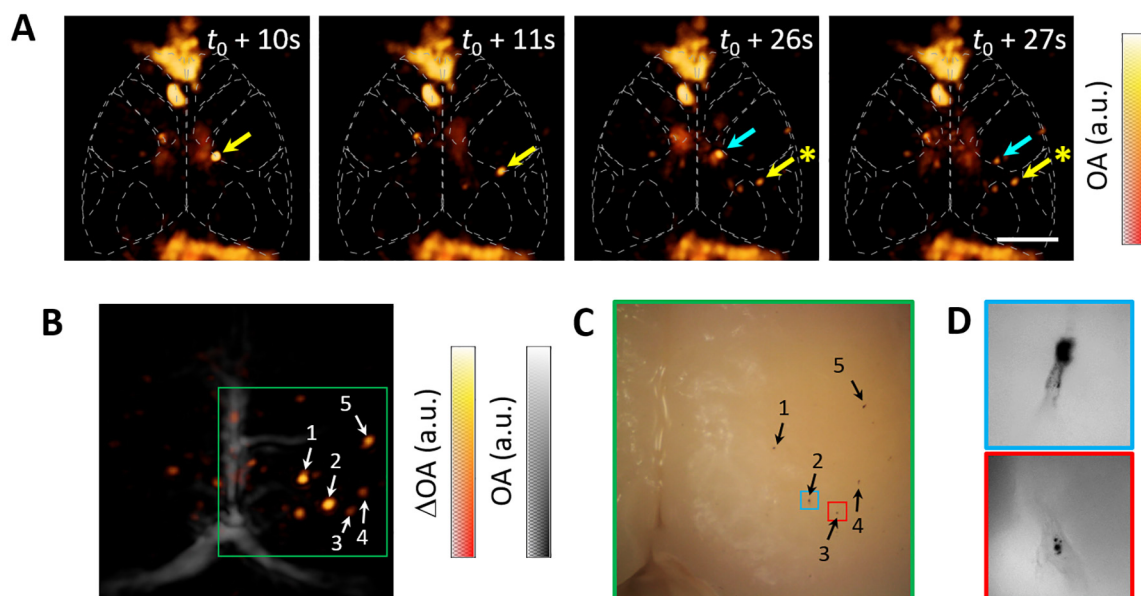
Fig. 3. Tracking of B16 cells in the mouse brain. (a) Maximum intensity projections (MIPs) of the three-dimensional optoacoustic images. Scalebar – 2 mm, t_0 indicates the time point when injection is started. (b) MIP of the optoacoustic image after background substraction (hot colormap) along with the MIP of the optoacoustic image before intracardiac perfusion (gray colormap). (c) Photograph of the excised brain for the green region indicated in (b). (d) Microscopic images of the red and blue regions indicated in (c) containing individual cells.

Discussion

The ability to follow the distribution and migration of metastatic cells is of vast importance for elucidating biological processes involved in tumor metastasis. To this end, the metastatic steps have been classified in two major phases, namely, physical translocation of cells from the primary tumor to a new microenvironment in distant tissues and cell proliferation and formation of a secondary tumor (colonization) [4]. The approach suggested herein offers the unprecedented capability to visualize the dynamics of cell transportation in entire macroscopic three-dimensional regions, providing new insights on how cells migrate and invade new tissues. From a clinical point of view, a better understanding of physical translocation of cells may find utility in preventing metastasis in patients diagnosed at an early stage and potentially define new therapeutic strategies in patients in which metastatic dissemination has been detected. Generally, the presence of cancer cells in the draining lymph nodes is the first indicator of metastasis. Metastatic melanoma cells have previously been observed with OA tomography in human sentinel lymph nodes at centimeter-scale depths [30]. Moreover, longitudinal tracking of tumor xenografts composed of cells synthesizing eumelanin via expression of tyrosinase has been performed with a high resolution OA imaging system [31].

The demonstrated feasibility to track B16 melanoma cells in the mouse brain allows addressing the critical question of whether volumetric OA tomography has sufficient sensitivity to detect flowing cells in living organisms. Yet, in our current experiments the blood was removed from the circulation while relatively large and highly-absorbing cells were employed. Visualizing the B16 melanoma cells in an intact animal can be made feasible if the blood background in the OAT images is eliminated to effectively amplify the signals from the cells. Spectral or temporal un-mixing approaches may aid this purpose [32–34], but challenged by pulse-to-pulse laser fluctuations and highly non-uniform light distribution in living tissues. Using higher frequency ultrasound arrays tailored to imaging of microvascular structures containing less blood than major vessels can also facilitate single cell detection [25]. Once the ultimate goal of tracking individual melanoma cells in deep tissues in the presence of blood is accomplished, the adaptation of the arrested cells to the new microenvironment and the growth of the secondary tumor can be studied in unperturbed *in vivo* environment. The observation of the initial colonization steps is challenged by the inefficiency of this process, since most of the cells experience apoptosis after extravasation or stay dormant for long periods of time [4]. It may also be possible to observe how cells intravasate the microvasculature of the lymph and blood systems, which is also an unlikely event to be captured. Detection of cells that are smaller or less absorbing than melanoma cells is additionally challenged by their lower OA detection thresholds. In general, the amplitude of the OA signals generated by a cell is proportional to the amount of light being absorbed, which generally scales with the cell volume, so that labelling may be required as in standard cell-tracking methods based on light microscopy [35]. Cell tracking is highly important for determining the distribution and long-term viability of biologically active cell populations in novel cancer therapeutic approaches such as adoptive immunotherapy or stem-cell therapy [36]. Cancer stem cells (CSC) appear to play an important role in cancer metastasis, which may be better understood if the dynamics of migration and differentiation of these cells can be effectively captured with a non-invasive high-resolution imaging modality. At a technical level, the demonstrated feasibility to detect individual absorbers flowing in vascular networks may find further use for enhancement of visibility and resolution of OA images via super-resolution and localization-based approaches [37–40].

All in all, optical methods based on endogenous or exogenous contrast are essential tools for unfolding the complex biological dynamics involved in cancer progression. While optical microscopy can resolve cellular and sub-cellular structures with high spatial resolution, the latter quickly deteriorates with depth due to light scattering in biological tissues. OA tomography has enabled breaking through this light diffusion limit by delivering high-resolution imaging of tumors at a whole-body scale in rodents [41–43]. Moreover, sub-micron spatial resolution in OA imaging can be achieved at <1 mm depths via optical focusing or using ultra-high-bandwidth ultrasound detectors [23,24], thus complementing information provided by fluorescence microscopy at the cellular level. Thereby, OA operates at a myriad of spatial scales ranging from organelles to organs with

a very versatile optical-absorption-based contrast [44]. Additionally, biological dynamics at multiple temporal scales ranging from milliseconds to hours or days can be covered with the method [45]. This unique capacity of optoacoustics may enable a more comprehensive view of cancer progression at spatial and temporal scales not covered by other modalities, with potential applicability in the clinical setting.

Methods

Optoacoustic imaging system

The spherical array (Imasonic SaS, Voray, France) used for optoacoustic tomographic imaging of the mouse brain was previously described [26]. Briefly, it consists of 512 piezocomposite elements densely distributed on a spherical surface with 40 mm radius and 140° (1.3π solid angle) angular coverage. Individual elements have 5 MHz central detection frequency and 100% −6 dB bandwidth. The array features a central cylindrical aperture with 8 mm diameter where light is delivered through a custom-made fiber bundle (Ceramoptec GmbH, Bonn, Germany). The output of an optical parametric oscillator (OPO) laser (Innolas GmbH, Krailling, Germany) providing ∼25 mJ (∼12 mJ at the output of the fiber bundle), <10 ns laser pulses at pulse repetition frequencies (PRFs) up to 100 Hz was coupled into the fiber. The wavelength of the laser can be tuned in the 700–900 nm range in a per-pulse basis. For animal imaging, the volume enclosed between the mouse head and the detection surface of the array was filled with agar. The agar block featured a cylindrical cavity coaxially aligned with the fiber bundle, which was filled with water to acoustically couple the mouse skin and reduce the light attenuation within agar. The beam diameter at the tissue surface was ∼8 mm, resulting in laser fluence <20 mJ/cm^2.

Intracardiac perfusion model

The intracardiac perfusion model was based on a recently-developed protocol [29]. Basically, intracardiac perfusion was performed after intraperitoneal (IP) injection of a mixture of 87.5 mg/kg Ketamine (Bremer Pharma, Wabing, Germany) and 12.5 mg/kg Xylazine (Bela-pharm, Vechta, Germany). 75 U of Heparin (Ratiofarm GbmH, Ulm, Germany) diluted in 100 ml 0.9% NaCl Solution (Braun AG, Melsungen, Germany) was also injected IP. The mouse was placed in supine position upon a silicon sheet with all extremities fixed with needles (Fig. 2a) and with the head fixed to a custom-made stereotactic holder (Narishige International Limited, London, UK). A second (lethal) dose of 87.5 mg/kg Ketamine and 12.5 mg/kg Xylazine was then injected IP. Access to the heart was ensured via removal of the ventral portion of the rib cage with an incision from the mid abdomen to the sternum. Freshly prepared artificial cerebrospinal fluid (ACSF) was supplied with Carbogen (Linde Group, Munich, Germany) and kept inside a Haake S7 water bath (ThermoFisher scientific Messtechnik GmbH, MÏnchen, Germany) set to 42 °C. A PLP3S perfusion pump (Bohr Labortechnik, DÏsseldorf) was used to transfer ACSF at a rate of 4.5–6 ml/min from its heated receptacle through a bubble trap, a glass heating coil (Radnoti LTD, Dublin, Ireland) and a physiological pressure transducer (AD Instruments, Sydney, Australia) connected to a pressure transducer Simulator/Tester (Utah Medical Products, Midvale, UT, USA). The flow continued through a 25G butterfly needle inserted in the left ventricle at an output temperature of 36.5–37.5 °C, while the right atrium was opened with an incision. The pressure of the pulsatile perfusion procedure was maintained below the physiological maximum of 100 mmHg by adjusting the pump rate. ACSF was pumped through the setup for at least 2 minutes before needle placement to remove any air bubbles within the set-up. After removal of blood via ACSF perfusion, the cells were added to the ACSF flow through a stop-

cock (Braun, Melsungen, Germany) via manual injection. All the animal experiments were carried out in accordance with the regulations of the Helmholtz Center Munich and with approval from the Government District of Upper Bavaria.

Cell culture and preparation

B16F10 murine melanoma cells were cultured in DMEM (Sigma-Aldrich) growth media supplemented with 10% fetal bovine serum and 1% Penicillin/Streptomycin and kept at 37°C and 5% CO_2. The cell lines were regularly checked for mycoplasma contamination and authenticity. For experimentation, an early cell passage was used to ensure strong intracellular melanin accumulation. Cells were detached using Trypsin/EDTA and washed twice with PBS buffer. Repeated gentle pipetting of cells as well as straining through a 35 µm mesh prior to injection in a PBS/2mM EDTA solution ensured single cell events. The average cell size of B16F10 was 16 µm as determined by the Countess Cell counter (Thermo Fisher Scientific, Waltham, Massachusetts, USA). 2.5 million cells diluted in 1 ml solution were intracardially injected in the mouse. This large amount of cells, much higher than typical concentrations of 1–10 cells/ml in vivo [46], was considered to ensure that circulating cells were detected in the limited region of interest covered by the three-dimensional OA imaging system.

Optical microscopic imaging of the isolated brain

The mouse brain was extracted (isolated) after the experiment. For this, an incision in the skull was performed with bone scissors and the upper skull plate, together with the brain, was carefully removed with forceps. The brain was carefully isolated with forceps in a Petri dish filled with ice-cold, oxygenated ACSF. Bright field images of the extracted brain were taken with Dino-Lite USB Mikroskop AD7013MZT (2592 × 1944 Pixel). Additionally, microscopic images with sub-cellular resolution of the arrested cells with higher magnification were taken on a Leica DMI 3000B inverted microscope with C Plan L40x/0.50 PH2 and L20x/0.40 objectives. The Leica application suite software was used to acquire the images. Due to their strong black contrast, the injected B16F10 cells were easily detectable before the white brain background. The unperturbed whole brain was imaged, thus facilitating the visualization of cells closer to the brain surface.

Author contributions

X.L.D.B, I.W and O.D. performed the experiments. X.L.D.B, I.W. and A.C.S. analyzed and processed the data. I.W. performed the cell culture and preparation of the cell lines. A.C.S. and D.R. validated the data analysis. X.L.D.B., I.W., A.C.S., V.N. and D.R. designed and supervised the study. All authors contributed to writing the manuscript.

Competing interests

The authors declare no competing interests.

Appendix A. Supplementary data

Supplementary data to this article can be found online at https://doi.org/10.1016/j.neo.2020.06.008.

References

1. Bandarchi B et al. *From melanocyte to metastatic malignant melanoma. Dermatol Res Practice* 2010;**2010**.
2. Uong A, Zon LI. Melanocytes in development and cancer. *J Cell Physiol* 2010;**222**(1):38–41.
3. Braeuer RR et al. Why is melanoma so metastatic? *Pigment Cell Melanoma Res* 2014;**27**(1):19–36.
4. Chaffer CL, Weinberg RA. A perspective on cancer cell metastasis. *Science* 2011;**331**(6024):1559–64.
5. Fein MR, Egeblad M. Caught in the act: revealing the metastatic process by live imaging. *Disease Models Mech* 2013;**6**(3):580–93.
6. Plaks V, Koopman CD, Werb Z. Circulating tumor cells. *Science* 2013;**341**(6151):1186–8.
7. Cabel L et al. Circulating tumor cells: clinical validity and utility. *Int J Clin Oncol* 2017;**22**(3):421–30.
8. Budd GT et al. Circulating tumor cells versus imaging—predicting overall survival in metastatic breast cancer. *Clin Cancer Res* 2006;**12**(21):6403–9.
9. Hengerer A, Grimm J. *Molecular magnetic resonance imaging. Biomed Imaging Intervention J* 2006;**2**(2).
10. Kirscher L et al. Doxycycline inducible melanogenic vaccinia virus as theranostic anti-cancer agent. *Theranostics* 2015;**5**(10):1045.
11. SundstrÖm T et al. Automated tracking of nanoparticle-labeled melanoma cells improves the predictive power of a brain metastasis model. *Cancer Res* 2013;**73**(8):2445–56.
12. DeÄn-Ben XL, Razansky D. Adding fifth dimension to optoacoustic imaging: volumetric time-resolved spectrally enriched tomography. *Light Sci Appl* 2014;**3**(1) e137.
13. Li L et al. Single-impulse panoramic photoacoustic computed tomography of small-animal whole-body dynamics at high spatiotemporal resolution. *Nat Biomed Eng* 2017;**1**(5):0071.
14. Úzbek A, DeÄn-Ben XL, Razansky D. Optoacoustic imaging at kilohertz volumetric frame rates. *Optica* 2018;**5**(7):857–63.
15. Lin H-CA et al. Characterization of cardiac dynamics in an acute myocardial infarction model by four-dimensional optoacoustic and magnetic resonance imaging. *Theranostics* 2017;**7**(18):4470.
16. Gottschalk S et al. Rapid volumetric optoacoustic imaging of neural dynamics across the mouse brain. *Nat Biomed Eng* 2019;**3**(5):392.
17. Zhang HF et al. Functional photoacoustic microscopy for high-resolution and noninvasive in vivo imaging. *Nat Biotechnol* 2006;**24**(7):848.
18. Weight RM et al. Photoacoustic detection of metastatic melanoma cells in the human circulatory system. *Opt Lett* 2006;**31**(20):2998–3000.
19. Galanzha EI et al. In vivo magnetic enrichment and multiplex photoacoustic detection of circulating tumour cells. *Nat Nanotechnol* 2009;**4**(12):855.
20. McCormack DR et al. Enhanced photoacoustic detection of melanoma cells using gold nanoparticles. *Lasers Surg Med* 2011;**43**(4):333–8.
21. Wei CW et al. Magnetomotive photoacoustic imaging: in vitro studies of magnetic trapping with simultaneous photoacoustic detection of rare circulating tumor cells. *J Biophotonics* 2013;**6**(6–7):513–22.
22. Strohm EM, Kolios MC. Classification of blood cells and tumor cells using label-free ultrasound and photoacoustics. *Cytometry Part A* 2015;**87**(8):741–9.
23. Strohm EM, Berndl ES, Kolios MC. High frequency label-free photoacoustic microscopy of single cells. *Photoacoustics* 2013;**1**(3–4):49–53.
24. Yao J, Wang LV. Sensitivity of photoacoustic microscopy. *Photoacoustics* 2014;**2**(2):87–101.
25. DeÄn-Ben XL, LÆpez-Schier H, Razansky D. Optoacoustic micro-tomography at 100 volumes per second. *Sci Rep* 2017;**7**(1):6850.
26. Mc Larney B et al. Uniform light delivery in volumetric optoacoustic tomography. *J Biophotonics* 2019 e201800387.
27. Jespersen SN, Òstergaard L. The roles of cerebral blood flow, capillary transit time heterogeneity, and oxygen tension in brain oxygenation and metabolism. *J Cereb Blood Flow Metab* 2012;**32**(2):264–77.
28. Sakadzõic¨ S et al. Large arteriolar component of oxygen delivery implies a safe margin of oxygen supply to cerebral tissue. *Nat Commun* 2014;**5**:5734.
29. Degtyaruk, O., et al. Optoacoustic Calcium Imaging of Deep Brain Activity in an Intracardially Perfused Mouse Brain Model. in Photonics. 2019. Multidisciplinary Digital Publishing Institute.
30. Stoffels I et al. Metastatic status of sentinel lymph nodes in melanoma determined noninvasively with multispectral optoacoustic imaging. *Sci Transl Med* 2015;**7**(317), p. 317ra199-317ra199.
31. Jathoul AP et al. Deep in vivo photoacoustic imaging of mammalian tissues using a tyrosinase-based genetic reporter. *Nat Photonics* 2015;**9**(4):239.
32. Cox BT et al. Quantitative spectroscopic photoacoustic imaging: a review. *J Biomed Opt* 2012;**17**(6) 061202.
33. Stiel AC et al. High-contrast imaging of reversibly switchable fluorescent proteins via temporally unmixed multispectral optoacoustic tomography. *Opt Lett* 2015;**40**(3):367–70.
34. Yao J et al. Multiscale photoacoustic tomography using reversibly switchable bacterial phytochrome as a near-infrared photochromic probe. *Nat Methods* 2016;**13**(1):67.
35. Sutton EJ et al. Cell tracking with optical imaging. *Eur Radiol* 2008;**18**(10):2021–32.
36. Kircher MF, Gambhir SS, Grimm J. Noninvasive cell-tracking methods. *Nat Rev Clin Oncol* 2011;**8**(11):677.
37. DeÄn-Ben XL, Ding L, Razansky D. Dynamic particle enhancement in limited-view optoacoustic tomography. *Opt Lett* 2017;**42**(4):827–30.
38. Chaigne T et al. Super-resolution photoacoustic imaging via flow-induced absorption fluctuations. *Optica* 2017;**4**(11):1397–404.
39. Dean-Ben XL, Razansky D. Localization optoacoustic tomography. *Light Sci Appl* 2018;**7**(4):18004.
40. Zhang P et al. In vivo superresolution photoacoustic computed tomography by localization of single dyed droplets. *Light Sci Appl* 2019;**8**(1):36.
41. McNally LR et al. Current and emerging clinical applications of multispectral optoacoustic tomography (MSOT) in oncology. *Clin Cancer Res* 2016;**22**(14):3432–9.
42. Taruttis A, van Dam GM, Ntziachristos V. Mesoscopic and macroscopic optoacoustic imaging of cancer. *Cancer Res* 2015;**75**(8):1548–59.
43. Ron A et al. Volumetric optoacoustic imaging unveils high-resolution patterns of acute and cyclic hypoxia in a murine model of breast cancer. *Cancer Res* 2019, p. canres. 3769.2018.
44. Wang LV, Hu S. Photoacoustic tomography: in vivo imaging from organelles to organs. *Science* 2012;**335**(6075):1458–62.
45. DeÄn-Ben X et al. Advanced optoacoustic methods for multiscale imaging of in vivo dynamics. *Chem Soc Rev* 2017;**46**(8):2158–98.
46. Kowalik A, Kowalewska M, GÆz¨dz¨ S. Current approaches for avoiding the limitations of circulating tumor cells detection methods—implications for diagnosis and treatment of patients with solid tumors. *Transl Res* 2017;**185**, p. 58–84. e15.